Polymer 105 (2016) 414–421

Contents lists available at ScienceDirect

Polymer

journal homepage: www.elsevier.com/locate/polymer

Nanograin nucleation at the growth front in melt crystallization of syndiotactic polystyrene

Chiu-Hun Su [a, b], Wei-Ru Wu [a], Chun-Yu Chen [a], Chun-Jen Su [a], Wei-Tsung Chuang [a], Kuei-Fen Liao [a], Su-Hua Chen [c], An-Chung Su [d], U-Ser Jeng [a, d, *]

[a] National Synchrotron Radiation Research Center, Science Park, Hsinchu, 30076, Taiwan
[b] Industrial Technology Research Institute, Hsinchu, 31040, Taiwan
[c] Department of Materials Science and Engineering, National Dong Hua University, Hualien, 97401, Taiwan
[d] Department of Chemical Engineering, National Tsing Hua University, Hsinchu 30013, Taiwan

ARTICLE INFO

Article history:
Received 30 April 2016
Received in revised form
8 July 2016
Accepted 12 July 2016
Available online 15 July 2016

Keywords:
Time-resolved SAXS/WAXS
β-crystalline lamellae
Syndiotactic polystyrene
Surface energy

ABSTRACT

Melt-crystallization of syndiotactic polystyrene (sPS) is studied using simultaneous small/wide angle X-ray scattering (SAXS/WAXS). Emergence, intensification, and saturation of WAXS reflections within 120 s at isothermal crystallization temperature T_c = 250 °C after quenching from 300 °C illustrate crystallinity development through successive nucleation of instantaneously stabilized crystallites of lateral ($hk0$) coherence length $\Lambda \approx 75$ nm. The corresponding SAXS profiles exhibit increased density heterogeneity due to formation of nanograins; fitting of time-resolved SAXS data with a model of arrayed disks reveals slightly thickened (l_c = 7.4–8.4 nm) disks of radius $R \approx 9$ nm and long period $L \approx 19$ nm with polydisperse stacking number slowly enhanced from an average of 1.2 to 2.4. The moderate ratio of $\Lambda/2R \approx 4$ indicates imperfect coalescence of nanograins in the lamellar assembly process. More importantly, with successively increased T_c from 250 to 260 °C the development of density heterogeneity of SAXS invariant Q_{inv} is found to precede that of the WAXS-determined crystallinity X_c increasingly more, suggesting a precursor mesophase with non-crystalline nanograins. Avrami analysis for the developments of X_c and Q_{inv} further reveals the same Avrami exponent $n \approx 3$, consistent with heterogeneous nucleation of crystallites; the corresponding Avrami rate constant $\kappa^{1/n}(T_c)$ extracted from X_c is correlated to the crystal growth rates $G(T_c)$ described by the Hoffman-Lauritzen theory with a common surface-nucleation rate constant K_g. A lateral surface energy $\sigma \approx 17$ mJ m^{-2} can be deduced on the basis of K_g using previously determined fold surface energy $\sigma_e \approx 27$ mJ m^{-2}. Correspondingly, $\kappa^{1/n}(T_c)$ extracted from Q_{inv} is described by a mesophase model proposed by Strobl with a zero-growth temperature of the nanograin mesophase ca. 30 K below the β-crystal melting point of sPS. Together, these results suggest that sPS melt-crystallization proceeds with nucleation of non-crystalline nanograins (SAXS-before-WAXS regime) at the crystal growth front, followed by crystallization of the nanograins with similar kinetics to sustain the growth front. Branching/twisting can occur at the lamellar growth front due to frustrated nanograin alignment, favoring the microscopically observed sheaf-like crystal morphology.

© 2016 Elsevier Ltd. All rights reserved.

1. Introduction

In the past decade, nanostructural features and the related kinetics of polymer crystallization have been better elucidated with increasingly enhanced time and spatial resolutions of synchrotron-based wide- and small-angle X-ray scattering (WAXS and SAXS) instruments [1,2]. The nucleation time and length scales that were used to establish the nucleation-dominated growth theories for polymer crystallization are now directly accessible for clarifying the classical theories and the often-referred phase separation mechanisms of spinodal decomposition and nucleation into mesomorphic domains prior to crystallization [3,4]. Accumulated experimental evidences with X-ray and light scattering observations have suggested some precursory ordering process prior to crystallization

* Corresponding author. National Synchrotron Radiation Research Center, 101Hsin-Ann Road, Hsinchu Science Park, Hsinchu, 30076, Taiwan.
E-mail address: usjeng@nsrrc.org.tw (U.-S. Jeng).

http://dx.doi.org/10.1016/j.polymer.2016.07.036
0032-3861/© 2016 Elsevier Ltd. All rights reserved.

under moderate-to-large supercooling [5–15]. Complementary to the scattering studies, microscopic techniques [15–17] have also demonstrated that lamellar crystals of polymers could comprise crystalline nodules of nanometer size. These evidences favor the polymer crystallization mechanism proposed by Strobl et al. [16,17] for a multistage process involving successive nucleation of nanograins at the growth front followed by stabilizing the nanograins into granular crystal blocks that further self-assembled into lamellae. Disfavoring the concept of mesomorphic nanograins, counter evidences were reported in parallel to support stem-wise nucleation at the crystal front by Lotz et al. [18,19] for a crystallization process proceeded by the classical nucleation and growth mechanism. In terms of physical interpretation, these two leading pictures of polymer crystallization differ mainly in the nucleating entities at the crystal front. Specifically, in the classical Hoffman scenario [19,20], growth at the crystal front is through stem-wise nucleation; in contrast, nucleation of nanograins (of preordered chains) is assumed in the Strobl's model [16,17]. In spite of the difference in the nucleating entities, the mathematical description of Hoffman's kinetic theory for polymer crystallization involves only thermodynamic parameters (rather than detailed molecular interactions) and may be equally applicable, after some modification, for the description of crystallization kinetics in terms the nanograin condensation model.

Previously, we have shown via several *cold*-crystallization studies of poly(9,9-di-*n*-octyl- 2,7-fluorene) [10], syndiotactic polystyrene (sPS) [11], poly(trimethylene terephthalate) [12,13], and poly(9,9-di-*n*-hexyl-2,7-fluorene) [14] of quenched polymer glasses that the nucleation process involves the emergence of mesomorphic embryos; within which, non-crystalline nanograins ranging from a few to couple ten nm in size can form [10–13], followed by their crystallization, thickening/growth, and coalescence upon inter-grain contact with increasing nanograin population. In the case of *melt*-crystallization, the nucleation density is presumably low in the early stage of crystallization, depending on the extent of supercooling. Yet, lamellar structure is often observed in the very early stage of melt crystallization process [6,21,22], suggesting an efficient nucleation strategy of the precursory nanograins in the early stage of melt-crystallization to stabilize the large density fluctuations before final transformation into the crystalline state. Here we report our observations on the nucleation and lamella formation process of β-crystals of sPS in melt crystallization upon quenching from equilibrated melt state. Using time-resolved SAXS and WAXS, we have simultaneously followed the isothermal formation of nanograins and their evolution into crystalline lamellae. A SAXS model of one-dimensionally (1D) stacking disks is further refined from previous studies [23–26] to extract the structural features of the nanograin assembly including thickness/lateral size of nanograins and lamellar spacing in the stacking process, in correlation with the SAXS invariant Q_{inv} and WAXS-determined crystallinity X_c [10–14]. Formation kinetics of β-crystalline nanograins is examined in the isothermal crystallization temperature (T_c) range of 250–260 °C. Avrami analyses with X_c and Q_c developments reveal similar formation kinetics with different origins. From the thermodynamics parameters hence obtained we further extract the lateral/fold surface energy values of the sPS nanograins as building blocks of crystalline lamellae and then correlate the anisotropic thermodynamic parameters to the sheaf-like lamellar morphology observed via scanning electron microscopy (SEM).

It is relevant to note that sPS has been extensively studied for nearly three decades due to its practical applications [27]. There are two main polymorphs coined as α and β phases for bulk-crystallized sPS in the absence of a solvent; both consist of all-*trans* chains [27]. The β phase is board-like, orthorhombic (space group $P2_12_12_1$) in structure, and comprises 4 chains in a unit cell of $a = 0.881$ nm, $b = 2.882$ nm, and $c = 0.506$ nm with $\rho = 1.067$ g cm^{-3} [11,28]. Isothermal crystallization at $T_c \geq 250$ °C results in mainly the thermodynamically stable β phase [11]. For simplicity, we have neglected further differentiations (β′ and β″ phases) from packing disorder [27].

2. Experimental details

2.1. Sample preparation

Syndiotactic polystyrene was received from the Grand Pacific Petrochemical, with weight-average molecular mass $M_w = 140$ kDa, polydispersity of 2.4, and high stereoregularity (>98%) [11]. The samples were purified via precipitation into methanol and consolidated under a protective nitrogen stream at 310 °C before quenching into ice water to give vitrified glass. The glassy sPS specimen (ca. 0.5–1.0 mm in thickness and 6 mm in diameter) was placed in an aluminum cell with Kapton windows ca. 4 mm in diameter for X-ray incidence. The sample cell was placed in a modified Mettler Toledo FP84 DSC holder, equilibrated at ca. 300 °C for 1 min, and then quenched to T_c between 250 and 260 °C within 1 min for isothermal crystallization [10,11].

2.2. X-ray measurements

With an 8 keV beam (0.5 mm in diameter, wavelength $\lambda = 0.155$ nm), time-resolved SAXS and WAXS data were simultaneously collected at the rate of 1 frame per 5 s throughout the isothermal crystallization process, using a MARCCD165 detector for SAXS and two 1D (gas-type; 20 cm in length) WAXS detectors, at the 23A SWAXS endstation of the National Synchrotron Radiation Research Center (NSRRC) [29]. The sample-to-detector distance (SD) was 1926 mm for the 2-D SAXS detector; SD values were 500 and 960 mm for the two WAXS detectors arranged in the vertical and horizontal directions, respectively, to cover a wider range of scattering angle. The scattering wavevector $q \equiv 4\pi\lambda^{-1}\sin\theta$ (where 2θ is the scattering angle) was calibrated using mixed silver behenate, sodalite, and silicon powders [29]. SAXS data were placed in the absolute scale (defined as the differential scattering cross section per unit volume, hence in units of cm^{-1}) according to established procedures [29].

2.3. Data analysis

SAXS scattering intensity profiles were modeled with

$$I(q) = n_p P(q) S(q) \tag{1}$$

where n_p is the number density, $P(q)$ the form factor, and $S(q)$ the structure factor of the scattering particles [30]. For disk-like particles with radius R and polydisperse thickness l, the normalized (i.e. $\tilde{P}(0) = 1$) and thickness-averaged form factor [31]

$$<\tilde{P}(q)> = \frac{\int G(q,l) V_p^2 f(l) dl}{\int V_p^2 f(l) dl} \tag{2}$$

is defined by the disk particle volume $V_p = \pi R^2 l$ and the spatial-orientation-averaged function

$$G(q,l) = \int_0^1 \left| \frac{2J_1(v)}{v} \frac{\sin(w)}{w} \right|^2 d\mu \quad (3)$$

with $v = QR(1-\mu^2)^{1/2}$ and $w = (1/2)Ql\mu$, where J_1 is the first order Bessel function [30]. The Schultz distribution function [30]

$$f(l) = [(z+1)/l_c]^{z+1}[l^z/\Gamma(z+1)]\exp[-(z+1)l/l_c] \quad (4)$$

was used to describe the polydisperse behavior of the disk thickness, where $l_c \equiv \langle l \rangle$ is the mean crystal thickness; the size polydispersity is defined by $p \equiv (\langle l^2 \rangle - l_c^2)^{1/2}/l_c = (z+1)^{-1/2}$ with $z\,(>-1)$ and the most-probable disk thickness $l_{mp} = zl_c/(z+1)$. Modified from that proposed previously [23–25], the structure factor for arrayed disks, comprising alternative crystalline and amorphous layers of layer thicknesses l_a and l_c, was approximated by

$$S_N(q) = 1 + (2/N)\sum_{k=1}^{N-1}(N-k)\cos(kqL)\exp\left(-k^2q^2\Delta_L^2/2\right) \quad (5)$$

with the stacking number N and the lamellar period $L\,(= l_a + l_c)$ of a disorder width Δ_L (resulted from the polydispersity in l_c and l_a) [23–25]. Polydispersity in N (assuming a Schultz distribution with integral values taken) for averaged $\langle S_N(q) \rangle$ was also included for improving data fitting. Combing Eqs. (1)–(5), the SAXS intensity for the polymer crystal lamellae is approximated by

$$I(q) = n_p(\Delta\rho)^2 < V_p^2 > \widetilde{<P(q)>} < S_N(q) > \quad (6)$$

with $\Delta\rho$ for the scattering contrast between crystalline and amorphous layers of the lamellae and $\langle V_p^2 \rangle$ for the averaged second moment of the scattering particle volume. Note that we have neglected the density difference between the amorphous zones outside (i.e. the matrix) and inside the lamellae in our SAXS data fitting. The scattering invariant $Q_{inv} = \int I(q)\, q^2\, dq$ within the experimental q-range was used to quantify the level of density heterogeneity in the approximated two-phase system (lamellae in the amorphous matrix) [10–13].

The relative crystallinity X_c, obtained from the WAXS profile based on the integrated intensity over the observed crystalline reflections, was normalized with respect to the *maximum* crystallinity observed [10–14]. Time-resolved $X_c(t)$ and $Q_{inv}(t)$ were analyzed on the basis of the Avrami-Erofeev expression [32,33].

$$\zeta(t) = 1 - \exp(-\kappa t^n) \quad (7)$$

where the extent of conversion $\zeta(t)$ at isothermal crystallization time t is characterized by the Avrami exponent n and rate constant $\kappa^{1/n}$ [32,33].

3. Results and discussion

3.1. Time-resolved WAXS/SAXS

Shown in Fig. 1a are the WAXS data collected during 250 °C isothermal crystallization of sPS after quenching from 300 °C. After an induction period of ca. 80s, emergences of weak WAXS peaks of (020), (110), (040), and (130) reflections of the β phase were observed (Fig. 1a) [11,34], which intensified and then plateaued consistently through the crystallization process (Fig. 1b). Interestingly, the crystal dimensions extracted from the peak widths (Fig. 1c) with the Scherrer equation [10–13] for the major (040) and (130) reflections indicate instantaneously saturated crystal size (or, coherence length) $\Lambda = 75$ (±15) nm without subsequent changes throughout the crystallization process (Fig. 1c), suggesting nucleation-dominated crystallization.

Concomitantly observed with the WAXS development is the marginally earlier increased SAXS scattering intensity at $t = 72$ s (Fig. 2a), which gradually gives rise to a broad lamellar hump over the isothermal crystallization as shown in Fig. 2b. The lamellar peak located at $q_c \approx 0.03$ Å^{-1} corresponds to a long period $L \approx 19$ nm; the growth behavior of SAXS invariant Q_{inv} synchronizes largely with that of WAXS-determined crystallinity crystals (as further detailed below) [10–13], suggesting closely correlated structural origins of crystallinity and density heterogeneity at $T_c = 250$ °C. Using the modified model for 1D arrayed disks detailed in Eqs. (1)–(6), we have fitted adequately the time-resolved SAXS profiles as that shown representatively in Fig. 2. We note that we have also tried other shapes with different sizes in the SAXS model fitting; however, the arrayed-disk model could best fit the data; the model (Eq. (5)) is intentionally developed to account for only 1D lamellar stacking of nanograins, but not including their lateral packing. The fitted parameters summarized in Fig. 3 reveal the marginally increased crystal thickness l_c from 7.2 nm to 8.3 nm together with the gradually developed lamellae (Fig. 3c and 3e), with the mean stacking number N_n increased slowly from 1.2 to 2.4 (Fig. 3b and 3e); whereas L (≈19 nm) remains approximately unchanged with $\Delta L = 4 \pm 1$ nm, throughout the crystallization process. As illustrated in Fig. 3b and 3e, the N_n values—close to but larger than unity—suggest formation of basically dispersed crystal nuclei together with a small population of coupled crystal nanograins, in the early stage of the melt crystallization (Fig. 2a).

Over the crystallization process N_n increases only moderately to 2.4 with moderately sharpened lamellar peak width (Fig. 2), despite the significantly enhanced Q_{inv}. In combination with the instantaneously matured nuclei ca. 75 nm in lateral dimension based on the WAXS peak widths (Fig. 1c), these SAXS features suggest that nucleation of β-crystals from (presumably fast) coalescence of a few primary nanograins (of nearly constant size $2R \approx 18$ nm and thickness $l_c \approx 8$ nm, cf. Fig. 3c,d) developed efficiently along the lamellar growth front, as compared to disk stacking in the perpendicular direction (with rather limited N_n values). The nearly constant L over the crystallization process implies lamellar formation via coupling of nearby condensed nanograins at an average interaction range of L.

3.2. Growth kinetics

To trace the crystallization growth kinetics, we have further measured similarly isotherm crystallization of sPS in the temperature range of 250–260 °C. Shown in Fig. 4a are growths of the relative crystallinity X_c extracted from the corresponding WAXS data (similar to that shown in Fig. 1a). These profiles show increasingly prolonged delays of the developments of X_c relative to that of Q_{inv} (Fig. 4c), as T_c increases (Fig. 4d). The SAXS-before-WAXS time $t_{s\text{-}w}$, defined by the preceding time of the overall Q_{inv} development profile to that of X_c (hence avoiding the ambiguity of smallest-Xc values detectable) is assigned to the regime of non-crystalline nanograins (Fig. 4d). The result is consistent with the previously reported phenomenon of an advanced SAXS lamellar peak before WAXS crystallization peaks [22]. Moreover, after the increasingly prolonged induction times with non-crystalline nanograins prior to observable crystallization (as T_c increase), X_c and Q_{inv} start to develop in synchrony. Specifically, after shifted by $t_{s\text{-}w}$ (Fig. 4d) the X_c profiles can overlap rather well with the corresponding Q_{inv} profiles. Both the corresponding X_c and Q_{inv} profiles can be fitted (Fig. 4a,b) respectively with a common Avrami index $n = 3.0 \pm 0.2$ and similar temperature-dependent Avrami rate

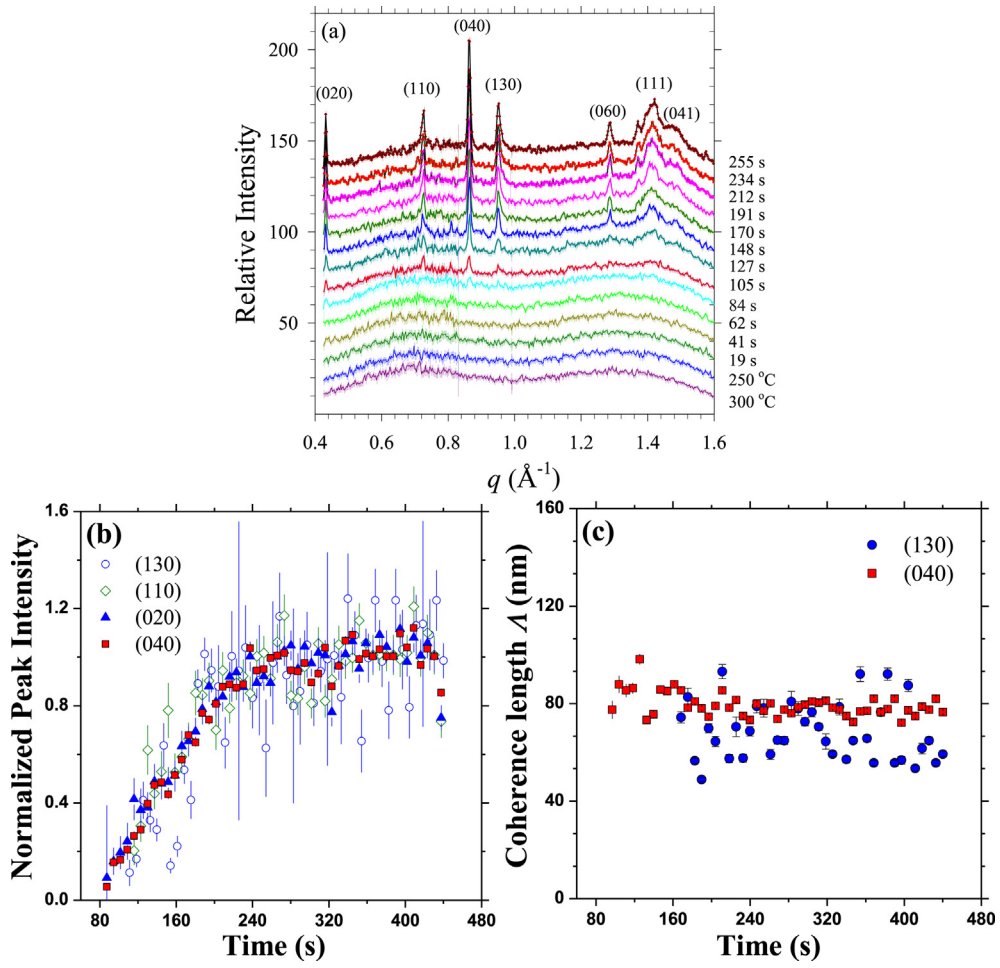

Fig. 1. (a) WAXS data of sPS collected during isothermal crystallization at 250 °C. (b) Synchronous growth of normalized peak area of main WAXS reflections. (c) Evolutions of the corresponding coherence lengths extracted from the widths of the respective reflections indicated.

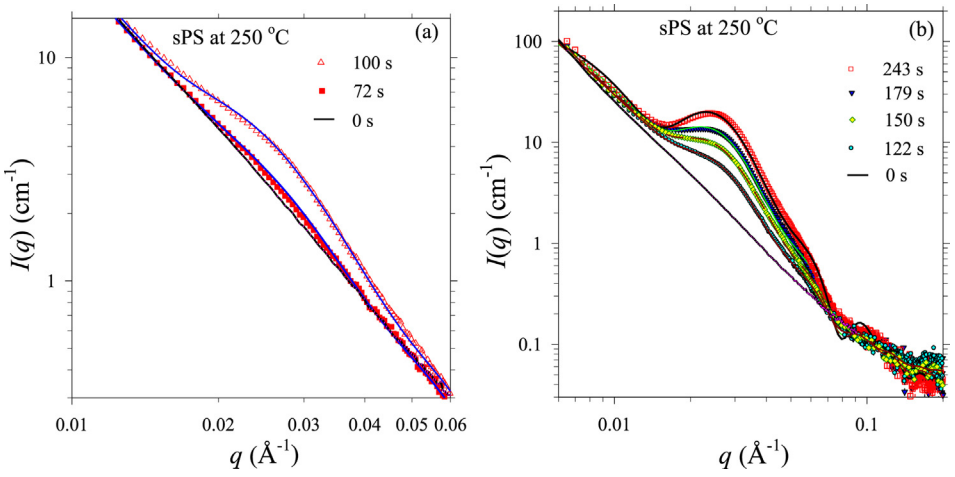

Fig. 2. Representative SAXS data measured at 250 °C sPS mlet crystallization during (a) 0–100 s and (b) 122–243 s. Data are fitted with the model of 1D arrayed disks. Note that a power-law scattering is also included in the fitting to take care of the scattering feature in the low-q region.

constants $\kappa(T_c)$ shown in Fig. 5 [32]. Hence, these results would suggest existence of growth fronts (most likely established with non-crystalline nanograins); with which, growth kinetics of X_c and can be regulated and synchronized to that of Q_{inv}. All these observations support the multistage model proposed by Strobl [16,17]: polymer crystals grow by a repeated nucleation of mesophase blocks at the growth face which transform into the final crystal blocks after a rapid spontaneous conversion.

Following a previous suggestion [32], we further correlate the extracted $\kappa^{1/n}$ values with the crystal growth rate $G(T_c)$ described by

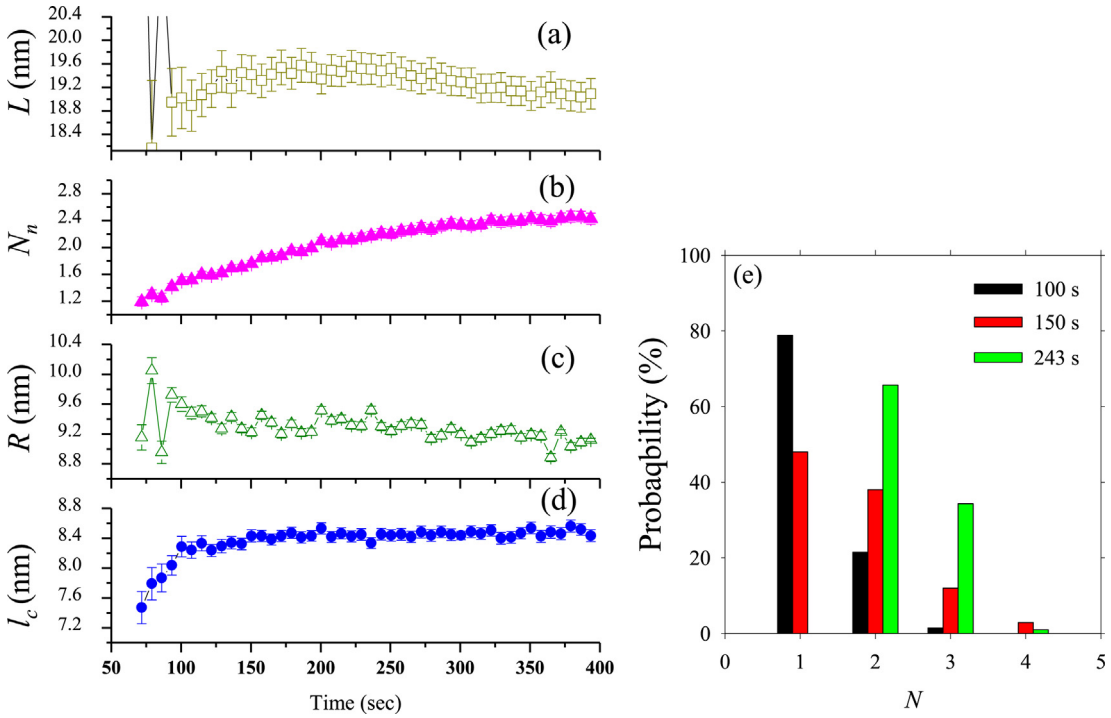

Fig. 3. Evolution of (a) the lamellar period L, (b) mean stacking number N_n, (c) radius R of the disk-like nanograins, and (d) the mean crystal thickness l_c during sPS melt crystallization at 250 °C obtained from the SAXS data fitting in Fig. 2. (e) Fitted distributions of the N values at the specific timings indicated.

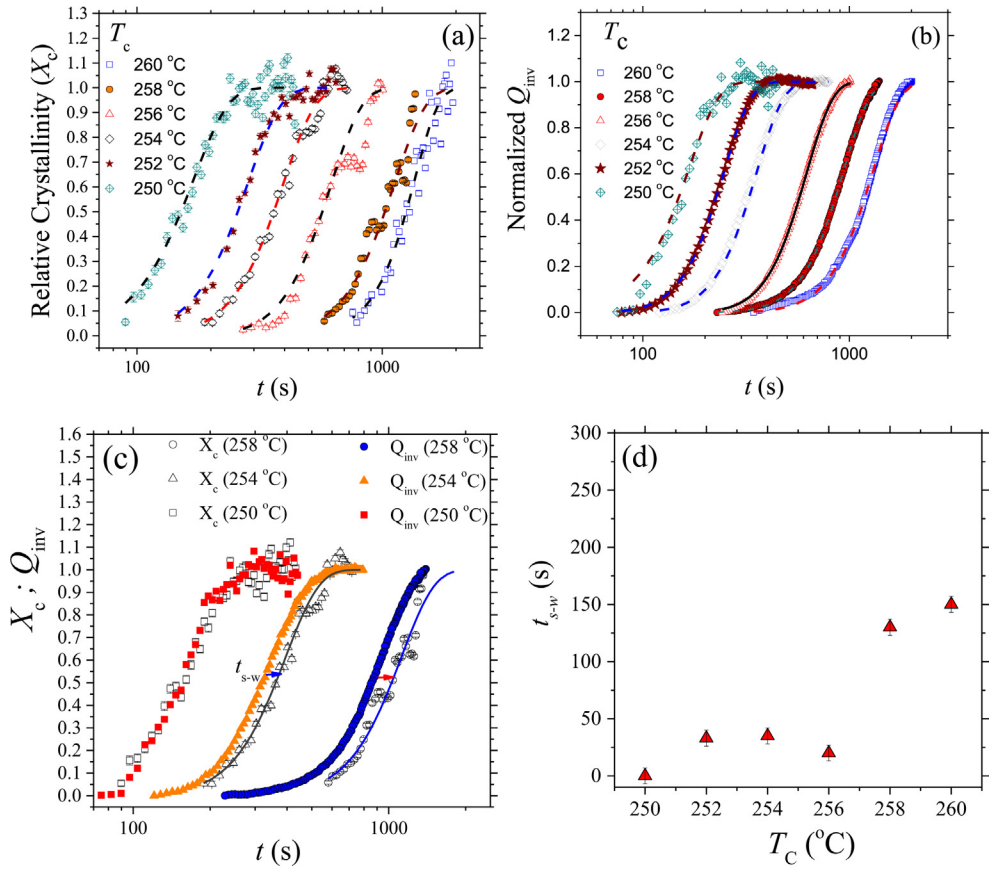

Fig. 4. Evolutions of (a) $X_c(t)$ and (b) $Q_{inv}(t)$ for melt-crystallization of sPS at T_c in 250–260 °C. Data are fitted with a common set of Avrami exponent $n = 3.0$ and growth rate constant $\kappa(T_c)$ shown in Fig. 5. (c) Representative comparisons of the X_c and Q_c profiles collected at the T_c indicated. Arrows indicate the preceding time $t_{s\text{-}w}$ (SAXS-before-WAXS) of the overall Q_{inv} profiles relative to that of X_c. (d) The T_c-dependent preceding time $t_{s\text{-}w}$.

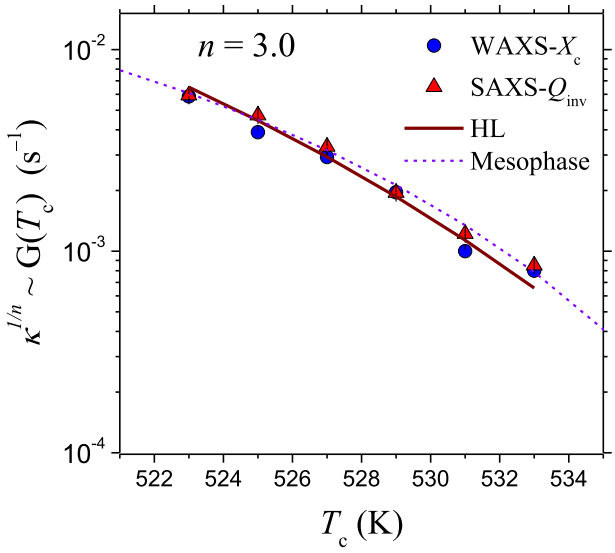

Fig. 5. Avrami rate constants $\kappa^{1/n}$ deduced respectively from X_c and Q_{inv} with a consistent exponent $n = 3.0$. The growth rates of X_c are fitted (solid curve) on the basis of the HL theory with T_m; whereas those of Q_{inv} are fitted (dotted curve) with the mesophase model with T_{zg}.

the Hoffman-Lauritzen (HL) equation [20,21], i.e.,

$$\kappa^{1/n} \equiv G(t) = G_o \exp\left[-U^*/R_g(T_c - T_\infty)\right] \exp\left[-K_g/(T_c f \Delta T)\right] \quad (8)$$

where U^* is the activation energy for segmental transportation [32,35,36], R_g the gas constant, $T_\infty = T_g - 30$ K (with T_g denoting the glass transition temperature) is the hypothetical temperature where motion associated with viscous flow ceases, K_g the nucleation constant, $\Delta T = T_m - T_c$ the supercooling with the equilibrium melting temperature T_m, and $f = 2T_c/(T_m + T_c)$ the correction factor for latent heat ΔH_f at large supercoolings [35,36]. In the HL theory,

$$K_g = n_g b_o \sigma \sigma_e T_m / k_B \Delta H_f \quad (9)$$

is defined by the regime-dependent factor n_g, layer thickness b_o, lateral surface energy σ, fold surface energy σ_e, the Boltzmann constant k_B, and ΔH_f [32,35,36]. Our WAXS results reveal nucleation-dominated crystallization (with immediately matured Λ) in the temperature range of 250–260 °C (Fig. 1), hence n_g is taken as 4, characteristic to regime III in the HL theory [20,21]. Shown in Fig. 5 are the $\kappa(T_c)^{1/n}$ values adequately fitted using Eq. (8) with a K_g value $= 7.5 \times 10^5$ K^2. In the data fitting, we have assumed a non-sensitive, constant activation energy U^* ($\approx$6.3 kJ mol^{-1}) as used in the previous studies [32,35,36].

With the fitted K_g value and the previously determined b_o (1.442 nm), σ_e (27 mJ m^{-2}), T_m (579 K), and ΔH_f (146 MJ m^{-3}) [34], the value $\sigma = 17$ (±1) J m^{-2} deduced is ca. 2/3 of the σ_e value, suggesting consistently a preferred nucleation at the growth front along the lateral direction of the crystalline β-nanograins. The work of chain folding $q_{cf} = 2a_o b_o \sigma_e$ deduced is 28 (±3) kJ mol^{-1}, with two sPS chains registering into the crystal lattice in pair to develop a layer thickness $b_o = 1.442$ nm and a stem width $a_o = 0.881$ nm in forming a significantly large cross-section of 1.27 nm^2. It should be noted that two folds are developed in a crystal stem with a cross-section area of $a_o b_o$, when the bilayer-constituent chains re-enter the crystal (namely the crystal lattice $b = 2.884$ nm). This q_{cf} value is comparable to $q_{cf} \approx 29$ kJ mol^{-1} reported previously for isotactic PS (iPS) [20]. However, the anisotropy $\sigma_e/\sigma = 1.6$ for 3D crystal packing of sPS is nearly three-times less than that ($\sigma_e/\sigma = 5.3$) of iPS (Table 1) [20]. Such dramatic difference renders different growth kinetics and crystal morphology of, such as, thicker crystals [37] and more features of spherulites observed in sPS melt crystallization (shown below) [38]. All the thermodynamic parameters obtained are summarized in Table 1.

On the other hand, the earlier appearance of Q_{inv} without X_c values (Fig. 4c) suggests a possibly lower U^* value in Eq. (8) for mesophase formation. Alternatively, as proposed in previous studies [17,39], the nucleation crystallization via the mesophase should be controlled by the supercooling below the melting point of the mesophase of zero growth temperature T_{zg} [17,39], rather than the supercooling below the crystal melting point (T_m) as formulated in the HL equation. The hence modified temperature dependence of the growth rate is

$$G = G_o \exp\left(-T_A^*/T_c\right) \exp\left[-T_G/(T_{zg} - T_c)\right] \quad (10)$$

where T_A^* is the effective activation temperature and the parameter T_G is defined by similar thermodynamics parameters as that for K_g in Eq. (9) in different dimensions [17,39]. With Eq. (10), we could fit the Avrami rate constants of Q_{inv} rather well as that shown in Fig. 5. The hence fitted $T_{zg} = 549 \pm 8$ K is 30 K below T_m (579 K) of the β phase of sPS; whereas T_G (100–300 K) and T_A^* (3650–5650 K) are strongly correlated and hence non-sensitively determined parameters in the data fitting [39]. Interestingly, the T_{zg} value obtained is reasonably close to the critical temperature T_Q (557 K) we estimated previously [34] for the thick crystal limit l_Q (9.6 nm) of sPS. We note that the extracted T_{zg} value of the mesomorphic state [39,40] thus provides a molecular explanation to the difficulty in having a crystal thickness over l_Q (an extrapolated crystal thickness from α and β crystal melting lines) [34] in bulk-crystallized specimens (i.e., a restriction to α-to-β phase transformation) owing to mesophase instability prior to T_m [34].

Table 1
Thermodynamic parameters extracted from melt-crystallization kinetics of sPS into β crystals at T_c = 250–260 °C in the current study and their melting behavior revealed in previous studies. Corresponding parameters in the case of isotactic PS (iPS) are also shown for comparison.

	T_m (K)	σ (mJ m^{-2})	σ_e (mJ m^{-2})	ΔH_f (MJ m^{-3})	q_{cf} (kJ mol^{-1})
sPS	579 (±2)[a]	17 (±1)	27 (±2)[a]	146 (±7)[a]	28 (±3)
iPS	562[c]/515[b]	6.6[b]	35[b]	91.1[b]	29[b]

[a] Taken from Table 2 in Ref. [34].
[b] Taken from Tables 1 and 2 in Ref. [20]; determined by the Hoffman-Weeks extrapolative method.
[c] Taken from Ref. [37]; determined by the Gibbs-Thomson melting line.

3.3. Morphological features from SEM

Growth behavior of sPS crystals is selectively observed with SEM, after isothermal crystallization for 180 s and 2 h, respectively, at 250 °C. In Fig. 6a and 6b, the SEM images taken after a short crystallization period exhibits relatively oriented but branched crystalline growth fronts. The approximately bundled but diverging growth fronts are consistent with limited stacking order in the perpendicular direction as revealed by the SAXS/WAXS results. The asymmetric development may be correlated with the significantly smaller lateral surface energy (and hence preferred nucleation sites) as compared to the fold surface energy associated with the lamellar stacking of β-crystalline nanograins. This anisotropy is presumably responsible for the sheaf-like crystal morphology observed after longer-term crystallization (Fig. 6c and 6d). It has been proposed by Gránásy et al. [41] that, with increasing

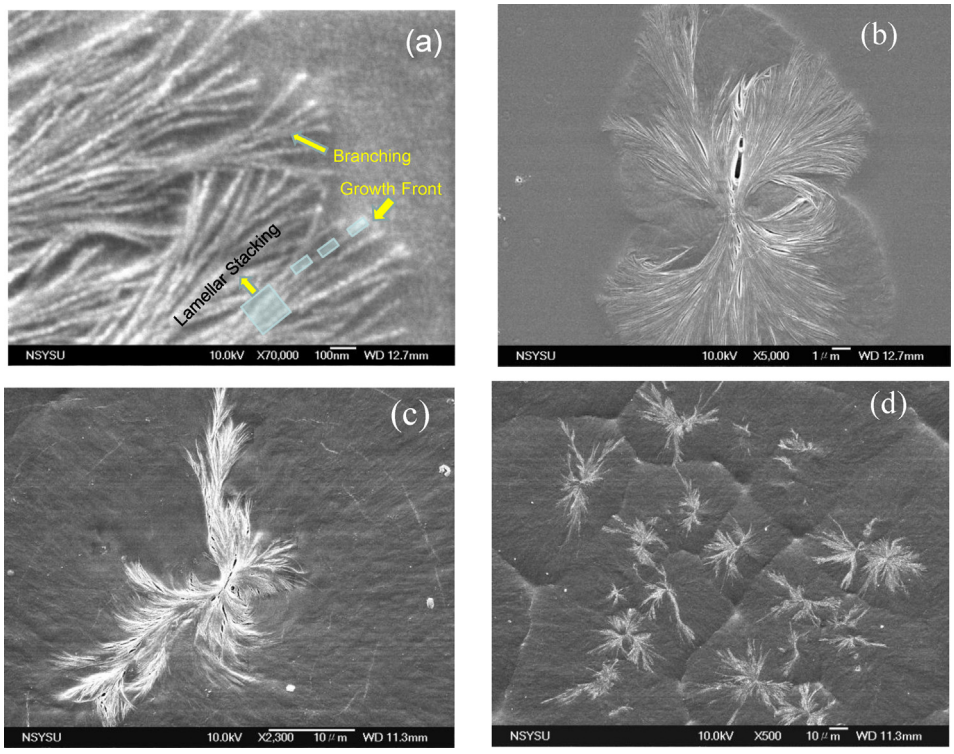

Fig. 6. SEM image taken for sPS under isothermal crystallization at 250 °C for (a, b) 180 s and (c, d) 2 h to show growth tips at high magnification and the globally sheaf-like features at low magnification. The arrows point to a typical growth front and a branching point, and the transparent block highlights the imperfect sideway packing of nano-granules. The scale bars are indicated at the bottoms of the figures for 100 nm, 1 μm, 10 μm, and 10 μm, respectively.

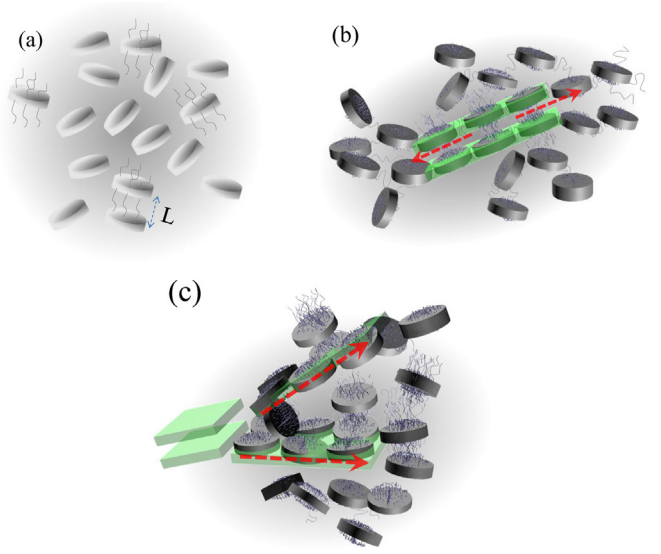

Fig. 7. (a) Formation of a cluster of non-crystalline nanograins (SAXS-before-WAXS regime). (b) Establishing a preferred growth front for efficiently crystallized and oriented nanograins (synchronized X_c and Q_{inv} regime). (c) A branching/twisting point at the lamellar growth front due to frustrated nanograin alignment.

branching probability at the crystal growth-front, the crystal growth pattern tend to shift from fibrils, sheaves, to spherulites. Along this line of argument, the sheaf-like morphology observed for sPS melt crystallization in the present T_c range may be correlated to the anisotropic ordering strengths (or surface energies), which regulate the alignment sequence/preference of the discrete local crystallographic symmetries and the orientation of nanograin nucleation at the growth front, hence, the branching frequency of the growth fronts.

Shown in Fig. 7 are cartoons that integrate the SAXS/WAXS and SEM results, illustrating the sPS melt crystallization features with initially sparsely formed non-crystalline nanograin clusters of a liquid-like ordering (SAXS-before-WAXS regime; Fig. 7a); which are followed by alignment of the nanograins for better established lamellar growth front along a preferred lateral direction (Fig. 7b). At the lamellar growth front, orientation-directed crystalline nanograins can be more efficiently formed (contributing to synchronized growths of X_c and Q_{inv}). Shown in Fig. 7c is a proposed branching occasion at the preferred growth front, where there are nanograins with frustrated orientation due to incompatible kinetics of rotational alignment; increasingly more branching points favor development towards spherulites.

4. Conclusion

Simultaneous SAXS/WAXS observations with the melt crystallization process of sPS at 250 °C reveals that the β-crystalline nanograins are nearly instantaneously perfected (within the probing time resolution of a few seconds) to lateral coherence of ca. 75 nm with a largely matured crystal thickness of ca. 7–8 nm in the early crystallization stage. Increase of the number of similar nanograins along the nucleation growth fronts, during the nucleation-dominated melt-crystallization process, is accompanied by gradually and weakly coupled nanograins for lamellae of a similar long period and a limited stacking number of 2–3. The collective developments of the crystallinity X_c and global density heterogeneity Q_{inv}, in the T_c range of 250–260 °C, are described by a common set of Avrami exponent n (≈3.0). The corresponding temperature dependent growth rate $\kappa(T_c)^{1/n}$ of X_c can be interpreted with the Hoffman-Lauritzen theory [42] for a consistent

nucleation-dominated crystal growth. The extracted lateral surface energy of about 2/3 of the fold surface energy for the β-crystals suggests a control factor in the development of crystal morphological features towards sheaves or spherulites. The growth rate $\kappa(T_c)^{1/n}$ of Q_{inv} is described by the mesophase model with a zero growth temperature proposed by Strobl. Our results suggest that, after initiation of non-crystalline nanograins, sPS melt-crystallization proceeds with continuous nucleation of non-crystalline nanograins at the crystal growth fronts, followed by crystallization of the nanograins with similar kinetics to sustain the growth fronts.

References

[1] T. Matsuura, M. Murakami, R. Inoue, K. Nishida, H. Ogawa, N. Ohta, T. Kanaya, Macromolecules 48 (2015) 3337–3343.
[2] T. Kanaya, I.A. Polec, T. Fujiwara, R. Inoue, K. Nishida, T. Matsuura, H. Ogawa, N. Ohta, Macromolecules 46 (2013) 3031–3036.
[3] D. Cavallo, D. Mileva, G. Portale, L. Zhang, L. Balzano, G.C. Alfonso, R. Androsch, ACS Macro Lett. 1 (2012) 1051–1055.
[4] D. Cavallo, G. Portale, L. Balzano, F. Azzurri, W. Bras, G.W. Peters, G.C. Alfonso, Macromolecules 43 (2010) 10208–10212.
[5] M. Imai, K. Kaji, T. Kanaya, Phys. Rev. Lett. 71 (1993) 4162–4165.
[6] E.L. Heeley, C.K. Poh, W. Li, A. Maidens, W. Bras, I.P. Dolbnya, A.J. Gleeson, N.J. Terrill, J.P.A. Fairclough, P.D. Olmsted, R.I. Ristic, M.J. Hounslow, A.J. Ryan, Faraday Discuss. 122 (2002) 343–361.
[7] K. Kaji, K. Nishida, T. Kanaya, G. Matsuba, T. Konishi, M. Imai, Adv. Polym. Sci. 191 (2005) 187–240.
[8] M. Imai, K. Kaji, Polymer 47 (2006) 5544–5554.
[9] J. Baert, P.V. Puyvelde, Macromol. Mater. Eng. 293 (2008) 255–273.
[10] C.H. Su, U. Jeng, S.H. Chen, S.J. Lin, Y.T. Ou, W.T. Chuang, A.C. Su, Macromolecules 41 (2008) 7630–7636.
[11] C.H. Su, U. Jeng, S.H. Chen, C.Y. Cheng, J.J. Lee, Y.H. Lai, W.C. Su, J.C. Tsai, A.C. Su, Macromolecules 42 (2009) 4200–4207.
[12] W.T. Chuang, W.B. Su, U.S. Jeng, P.D. Hong, C.J. Su, C.H. Su, Y.C. Huang, K.F. Laio, A.C. Su, Macromolecules 44 (2011) 1140–1148.
[13] J.-B. Jheng, W.-T. Chuang, P.-D. Hong, Y.-C. Huang, U. Jeng, C.-J. Su, G.-R. Pan, Polymer 54 (2013) 6242–6252.
[14] W.R. Wu, W.T. Chuang, U.S. Jeng, C.J. Su, S.H. Chen, C.Y. Chen, C.H. Su, A.C. Su, Polymer 53 (2012) 3928–3936.
[15] S.H. Chen, H.L. Chou, A.C. Su, S.A. Chen, Macromolecules 40 (2007) 5353–5359.
[16] M. Grasruck, G. Strobl, Macromolecules 36 (2003) 86–91.
[17] G. Strobl, Rev. Mod. Phys. 81 (2009) 1287–1300.
[18] B. Lotz, Eur. Phys. J. E 3 (2000) 185–194.
[19] B. Lotz, Adv. Polym. Sci. 180 (2005) 17–44.
[20] J.D. Hoffman, R.L. Millerr, H. Marand, D.B. Roitman, Macromolecules 25 (1992) 2221–2229.
[21] J.D. Hoffman, G.T. Davis, in: N.D. Hanny (Ed.), Treatise in Solid State Chemistry, 3, Plenum, New York, 1975, pp. 497–614. Ch.7.
[22] E.L. Heeley, A.V. Maidens, P.D. Olmsted, W. Bras, I.P. Dolbnya, J.P.A. Fairclough, N.J. Terrill, A.J. Ryan, Macromolecules 36 (2003) 3656–3665.
[23] H.K. Huang, H.S. Sheu, W.T. Chuang, U.S. Jeng, A.C. Su, W.R. Wu, K.F. Liao, C.Y. Chen, S.Y. Chang, H.M. Lai, IUCrJ 1 (2014) 418–428.
[24] D. Richter, D. Schneiders, M. Monkenbusch, L. Willner, L.J. Fetters, J.S. Huang, M. Lin, K. Mortensen, B. Farago, Macromolecules 30 (1997) 1053–1068.
[25] M. Shibayama, T. Hashimoto, Macromolecules 19 (1986) 740–749.
[26] R.J. Roe, Methods of X-ray and Neutron Scattering in Polymer Science, Oxford University Press, Oxford (, 2000.
[27] E.M. Woo, Y.S. Sun, C.P. Yang, Prog. Polym. Sci. 26 (2001) 945–983.
[28] L. Cartier, T. Okihara, B. Lotz, Macromolecules 31 (1998) 3303–3310.
[29] U. Jeng, C.H. Su, C.J. Su, K.F. Liao, W.T. Chuang, Y.H. Lai, J.W. Chang, Y.J. Chen, Y.S. Huang, M.T. Lee, K.L. Yu, J.M. Lin, D.G. Liu, C.F. Chang, C.Y. Liu, C.H. Chang, K.S. Liang, J. Appl. Crystallogr. 43 (2010) 110–121.
[30] S.H. Chen, T.L. Lin, in: K. Sköld, D.L. Price (Eds.), Methods in Experimental Physics -Neutron Scattering in Condensed Matter Research, 23B, Academic, New York, 1987, pp. 489–543. Ch.16.
[31] E.Y. Sheu, Phys. Rev. A 45 (1992) 2428.
[32] C. Wang, W.P. Liao, M.L. Wang, C.C. Lin, Polymer 45 (2004) 973–981.
[33] Y.H. Lai, S.W. Cheng, S.W. Chen, J.W. Chang, C.J. Su, A.C. Su, H.S. Sheu, C.Y. Mou, U.S. Jeng, RSC Adv. 3 (2013) 3270–3283.
[34] C.H. Su, U. Jeng, S.H. Chen, C.Y. Cheng, J.J. Lee, Y.H. Lai, W.C. Su, J.C. Tsai, A.C. Su, Macromolecules 42 (2009) 4200–4207.
[35] J.M. Huang, F.C. Chang, J. Polym. Sci. Part B Polym. Phys. 38 (2000) 934–941.
[36] S. Vyazovkin, N. Sbirrazzuoli, Macromol. Rapid Commun. 25 (2004) 733–738.
[37] M. Al-Hussein, G. Strobl, Macromolecules 35 (2002) 1672–1676.
[38] T. Liu, J. Petermann, C. He, Z. Liu, T.-S. Chung, Macromolecules 34 (2001) 4305.
[39] T.-Y. Cho, W. Stille, G. Strobl, Colloid. Polym. Sci. 285 (2007) 931–934.
[40] G. Strobl, Prog. Polym. Sci. 31 (2006) 398–442.
[41] L. Gránásy, T. Pusztai, G. Tegze, J.A. Warren, J.F. Douglas, Phys. Rev. E 72 (2005) 011605.
[42] J.D. Hoffman, Robert L. Miller, Polymer 38 (1997) 3151–3212.